

Silicene: Wet-Chemical Exfoliation Synthesis and Biodegradable Tumor Nanomedicine

Han Lin, Wujie Qiu, Jianjun Liu, Luodan Yu, Shanshan Gao, Heliang Yao, Yu Chen,* and Jianlin Shi*

Silicon-based biomaterials play an indispensable role in biomedical engineering; however, due to the lack of intrinsic functionalities of silicon, the applications of silicon-based nanomaterials are largely limited to only serving as carriers for drug delivery systems. Meanwhile, the intrinsically poor biodegradation nature for silicon-based biomaterials as typical inorganic materials also impedes their further in vivo biomedical use and clinical translation. Herein, by the rational design and wet chemical exfoliation synthesis of the 2D silicene nanosheets, traditional 0D nanoparticulate nanosystems are transformed into 2D material systems, silicene nanosheets (SNSs), which feature an intriguing physiochemical nature for photo-triggered therapeutics and diagnostic imaging and greatly favorable biological effects of biocompatibility and biodegradation. In combination with DFT-based molecular dynamics (MD) calculations, the underlying mechanism of silicene interactions with bio-milieu and its degradation behavior are probed under specific simulated physiological conditions. This work introduces a new form of silicon-based biomaterials with 2D structure featuring biodegradability, biocompatibility, and multifunctionality for theranostic nanomedicine, which is expected to promise high clinical potentials.

Silicon, the most abundant element of the Earth's crust after oxygen, is an essential, nontoxic, environmentally friendly, biocompatible, and ubiquitous chemical element in living system and industrial applications. Silicon has not only been shown to elevate plant-cell wall strength and structural integrity in plant, but also plays an indispensable role in human health.^[1] Silicon is necessary for the synthesis of collagen and elastin, which are the main components of aorta in the human body, is also an essential constituent in organs and tissues such as hair, bone,

Dr. H. Lin, Dr. W. Qiu, Dr. J. Liu, Dr. L. Yu, Dr. S. Gao, H. Yao, Prof. Y. Chen, Prof. J. Shi
State Key Laboratory of High Performance Ceramics and Superfine Microstructures
Shanghai Institute of Ceramics
Chinese Academy of Sciences
Shanghai 200050, P. R. China
E-mail: chenyu@mail.sic.ac.cn; jlshi@mail.sic.ac.cn

Dr. H. Lin, Dr. S. Gao
Center of Materials Science and Optoelectronics Engineering
University of Chinese Academy of Sciences
Beijing 100049, P. R. China

 The ORCID identification number(s) for the author(s) of this article can be found under <https://doi.org/10.1002/adma.201903013>.

DOI: 10.1002/adma.201903013

or skin.^[2] Porous silicon (pSi) is a specific and vitally important form of the chemical element silicon, featuring intrinsic bioactivity, superhydrophobicity, and luminescence properties coupled with the large surface to volume ratio rendered by pore microstructure, which has provided considerable potentials for optoelectronics, sensors, biomedicine, and even a battery anode.^[3] Silica is the most popular oxidized form of chemical element silicon, among which, especially, mesoporous silica shows broad application potentials in medicine, industrial catalysis, energy storage, and imaging.^[4] Nonetheless, the diversity of silicon topology brings no increment for the single-component silicon on physiochemical properties, which impedes interdisciplinary research based on silicon materials.

As the third topology of silicon materials, 2D silicene differs strikingly from other silicon materials such as pSi or silica,^[5] featuring unique physiochemical virtues like Quantum spin Hall effect,^[6] giant magnetoresistance,^[7] and chiral superconductivity^[8] by its unique low-buckled topography. To date, silicene material has been fabricated by physical vapor deposition (PVD) method on a variety of substrates.^[9] The first synthesis of monolayer silicene was achieved on Ag(111) surface.^[10] Besides, other studies have achieved silicene growth on Ir(111),^[5c] MoS₂,^[11] ZrC(111),^[12] and ZrB(001)^[13] substrates under ultrahigh vacuum (UHV) ambience. However, these as-synthesized silicene derived from epitaxial growth methods encounter three major drawbacks: scalable synthesis limitation, nonuniformity in vertical scale, and great difficulties in the transfer of layered materials from substrates.^[14] Given that the same dilemma has impeded the research advances and practical application of 2D materials such as transition metal carbides nanosheets (MXene),^[15] the chemical vapor deposition (CVD) approach could only be utilized to grow α -Mo₂C MXene, but exhibited the limitations of low-yield production and substrate dependence.^[16] Fortunately, these issues have been overcome by using selective extraction method upon converting MAX-phase layered compounds to versatile 2D MXene-phase nanosheets.^[17] By analogy, 2D silicene, a hexagonal honeycomb lattice featuring non-planar buckled configuration, could be supposedly synthesized from the precursor Zintl-phase silicide (e.g., CaSi₂) via a topochemical deintercalation process of selective Ca-removal.

So far, the current experimental efforts in the 2D silicene synthesis by chemical manipulation are still suffering 2D silicene applications from the free-standing morphology, large-scale production, and high-quality flakes.^[18] Despite the recent progress in the exploration of electronic properties of silicene, there has been no reports that could be found to date on the applications of 2D silicene nanomaterials in biomedical field. Herein, we report the wet-chemical synthesis and biomedical performances of 2D silicene, as the next-generation silicon-based biodegradable phototherapeutic agent, together with temporal/thermo-dependent degradation behavior attributing to its high photothermal-conversion performance, desirable photoacoustic effect, and intriguing ambience-triggered biodegradation. The high photothermal therapeutic capacity, intrinsic high biocompatibility of silicon component, and the desirable biodegradative nature of 2D silicene give great promises for broadening the biomedical use of silicon-based nanoplateforms and their further clinical translation.

The 2D silicene nanosheets were synthesized via a mild oxidation and delamination process based on wet chemistry mechanism, which was an analogue strategy reported by our and other groups for 2D MXene fabrication.^[17a,18c] In brief, the precursor Zintl phase CaSi_2 crystals were subject to a mild oxidation process in anhydrous acetonitrile (CH_3CN), together with a weak oxidant, iodine (I_2). Based on the layered binary silicide CaSi_2 , alternately consisting of planar Ca layers and buckled Si layers, the Si layers were oxidized by I_2 through an outer to inner diffusion process, and the by-product CaI_2 was well dissolved in solvent CH_3CN simultaneously. These as-prepared multilayered silicene (ML silicene) nanosheets exhibit accordion-like microstructure. In order to thoroughly exfoliate the freestanding silicene nanosheets, the ML silicene nanosheet precipitate was thermo-expanded at $380\text{ }^\circ\text{C}$, and subsequently immersed into the liquid N_2 (L-N_2) (quenching to $-196\text{ }^\circ\text{C}$) until the complete evaporation of L-N_2 in the container. The freestanding silicene nanosheets, few- or single-layered silicene (FL silicene), were peeled off by the L-N_2 gasification (Figure 1a). The few- or single-layered silicene fabricated by this efficient strategy features high-quality sheet and freestanding morphology with scalable production potentials, probably meeting the ever-strict needs in, such as, biomedical application or electronic device fabrications (Figure 1b).

Scanning electron microscopy (SEM) images exhibit that the Zintl phase CaSi_2 features the specific structure of a layered binary compound, promising the potential to extract Si layers from the layered parent CaSi_2 (Figure 1c and Figure S1, Supporting Information). High-resolution transmission electron microscopy (HRTEM) imaging clearly demonstrates that the pristine CaSi_2 consists of alternating $[\text{Ca}]_n^+$ layers and buckled honeycomb $[\text{Si}]_n^-$ layers in atomic resolution (Figure 1d). Indeed, these silicene sheets feature a lower symmetry and pseudo-planar flatland structure differing strikingly from that of graphene of planar hexagonal rings. The corresponding element mapping further confirms that these alternating 2D silicene buckled sheets are separated from each other by planar monolayer of Ca (Figure 1e,f).^[9] The selected area electron diffraction (SAED) pattern shows that the pristine CaSi_2 possesses a rhombohedral ($R\bar{3}m$) structure (Figure 1g). After the “gentle” oxidation by I_2 , the Ca layers were extracted out of calcium

silicide bulks with the by-product CaI_2 being well dissolved in CH_3CN . The secondary electron SEM imaging gives the precise message about morphology and surface topography, which exhibit the typical layered morphology of silicene structure after Ca-layer removal, proving the efficient deintercalation of individual grains and the uniform stack-up of the silicene sheets (Figure 1h,i).

TEM images further depict the electron-transparent morphology and a well-stacked microstructure of ML silicene (Figure 1j). HRTEM image and the corresponding SAED pattern clearly exhibit crystalline lattice of ML silicene nanosheets with unchanged hexagonal structure (Figure 1k,l). After several cycles of rapid quenching and gas-exfoliation process, the bright-field and dark-field TEM images corroborate that the prepared few- or single-layered silicene nanosheets are ultrathin and almost electron-transparent (Figure 1m,n), which feature the typical 2D stand-alone morphology. The elemental mapping of silicene nanosheets exfoliated from Zintl phase precursor clearly suggests the efficient removal of Ca layer (Figure 1o). The HRTEM image reveals the well-crystallized feature of silicene nanosheets with hexagonal structure, and the corresponding original SAED pattern also indicates the preserved well-defined hexagonal structure (Figure 1p,q), revealing the disappearance of the most intense peaks of Nb_2AlC at $2\theta \approx 39^\circ$ because of the exfoliation. The energy dispersive spectroscopic analyses for CaSi_2 and final product silicene reveal the disappearance of intense peaks of Ca element because of the exfoliation, demonstrating the complete removal of Ca atoms in the product of silicene and the inexistence of Ca-related by-products like CaI_2 or CaSi_2 residuals (Figure S2, Supporting Information). The small amount of oxygen measured by EDS is due to the partial surface oxidation during the characterization process, which would be hard to remove completely.

To further determine the composition and microstructure of 2D silicene nanosheets, Raman spectroscopy was adopted (Figure S3, Supporting Information). Generally, the Raman frequencies of 2D sheets produced from Zintl phase precursor contain the out-of-plane vibrational mode (A_{1g}) and in-plane vibrational mode (E_{2g}).^[19] The vibrational mode A_{1g} , a vertical buckling in the nonplanar corrugated configuration of silicene, responds to the asymmetric shoulder in the Raman shift ranging from 450 to 500 cm^{-1} (Mode A_{1g}), which well matches the typical silicene vibrations via epitaxial synthesis, and is, in contrast, absent in bulk sp^3 silicon and pristine CaSi_2 .^[5a] In addition, the sharp and intense peak ($515\text{--}522\text{ cm}^{-1}$), a fingerprint Raman vibrational mode of silicene, dominated by the symmetric stretching of Si–Si interactions in planar hexagonal rings (E_{2g} vibrational mode), suggests the integrity of the silicene nanosheets.^[10c] The measured Raman spectrum confirms the pseudo-planar flatland in silicene and the integrity of basal plane hexagonal symmetry in silicene layered microstructure. The X-ray photoelectron spectroscopic (XPS) analyses of Zintl phase CaSi_2 and exfoliated silicene nanosheets in the Ca 2p region verify the absence of Ca-related peaks after silicene delamination (Figure S4a,c, Supporting Information), also confirming the complete removal of Ca atoms in the product of exfoliated silicene nanosheets and inexistence of Ca-related by-products like CaI_2 or residual CaSi_2 precursor. The Si 2p peak at a binding energy around 99.4 eV is consistent with

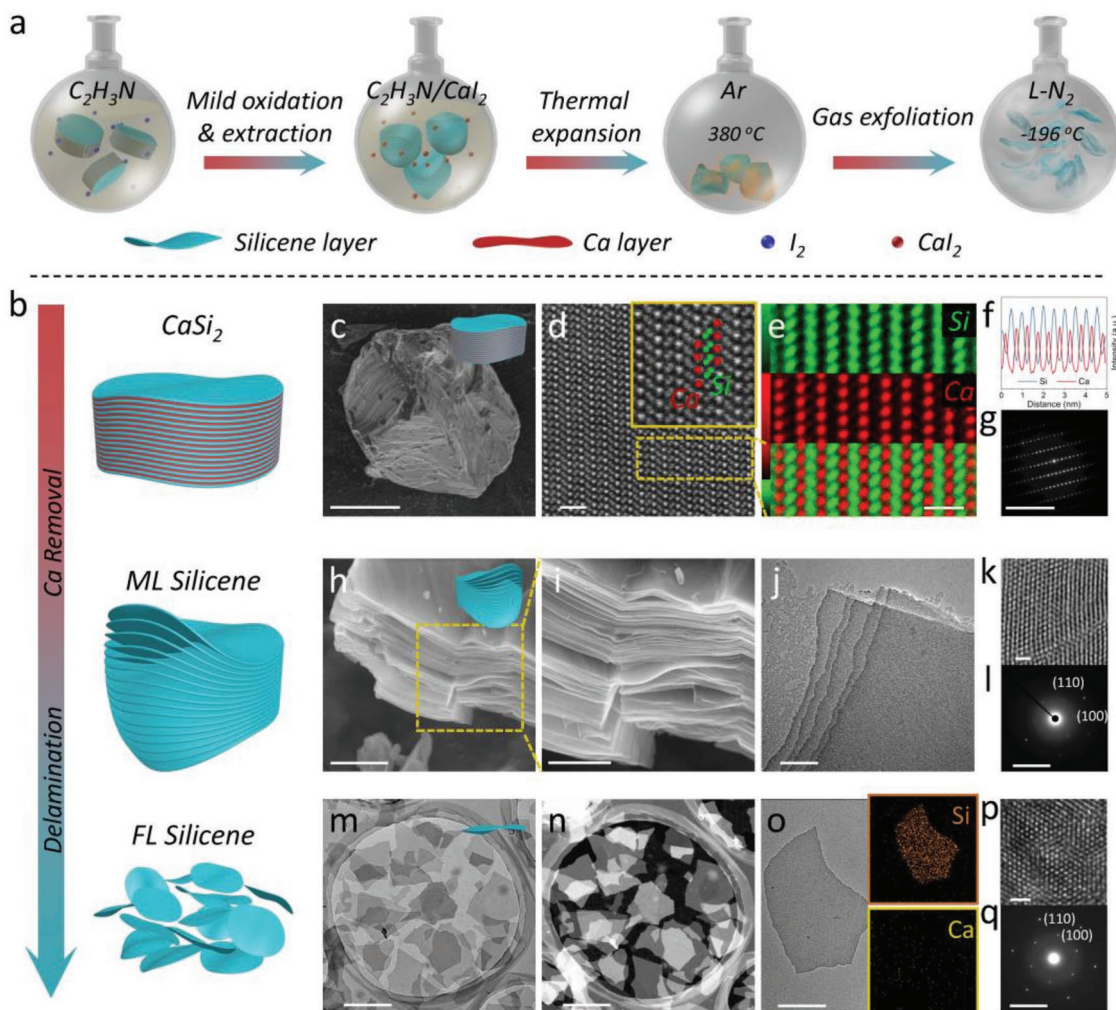


Figure 1. Synthesis and characterization of 2D silicene nanosheets. a) Scheme for the synthesis of 2D silicene nanosheets. b) Schematic diagram of silicene nanosheet exfoliation process including mild oxidation and ultrasound delamination. c) SEM images of pristine CaSi_2 . d) HR-STEM image, e) elemental mapping, f) corresponding element-linear scanning profiles and g) SAED pattern of CaSi_2 . Scale bars, 5 μm (c); 1 nm (d); 1 nm (e); 10 nm^{-1} (g). h, i) SEM images, j) TEM image, k) HRTEM image and l) corresponding SAED pattern of multilayer silicene. Scale bars, 2 μm (h); 1 μm (i); 50 nm (j); 1 nm (k); 5 nm^{-1} (l). m) Bright-field and n) dark-field TEM image of few- or single-layered silicene nanosheets. o) Elemental mapping, p) HR-STEM image and q) the corresponding SAED pattern of as-synthesized silicene nanosheets. Scale bars, 0.5 μm (m,n); 100 nm (o); 1 nm (p); 5 nm^{-1} (q).

the reported Si^0 2p peaks in silicene (Figure S4b,d, Supporting Information).^[18c] Atomic force microscopy (AFM) measurement provides further evidence for the typical 2D sheet morphology of freestanding silicene nanosheets (Figure S5a,b, Supporting Information). The statistical lateral size is statistically distributed from 50 to 350 nm, indicating the consistency with the TEM characterizations (Figure S5c, Supporting Information). In addition, Figure S5d in the Supporting Information clearly exhibits a planar structure of silicene nanosheets with a monolayer thickness of 0.6 nm similar to graphene. In fact, the as-obtained silicene nanosheets contain monolayer, two-layer and three-layer structures with the typical thickness ranging from 0.3 to 1.8 nm.

Degradation performance of inorganic nanoagents is still one of the major obstacles in their clinical-translations. Thus, the investigation of oxidation/degradation nature of silicene under

ambient conditions is of great significance in exploiting its future biomedical applications. To evaluate the biodegradability of silicene nanosheets (noted as SNSs), SNSs dispersions were dispersed in water (exposed to the air) at room temperature (RT) for 14 days and then their optical/spectroscopic properties, chemical structure, and microscopic morphology changes were analyzed at varied time intervals (0, 3, 7, and 14 days). The color of the SNSs suspension became weaker over time, and the suspension changed to a nearly translucent solution in 14 days (Figure 2a).

The corresponding visible–near-infrared (vis–NIR) absorption spectra of SNSs suspension exhibit the significantly decreased absorbance intensity with the increasing time duration of dispersion (Figure 2b and Figure S8, Supporting Information),^[20] and the extinction coefficient (ϵ) of the biodegrading SNSs suspension was plotted as a function of time, demonstrating an exponential decay behavior, i.e., marked degradation,

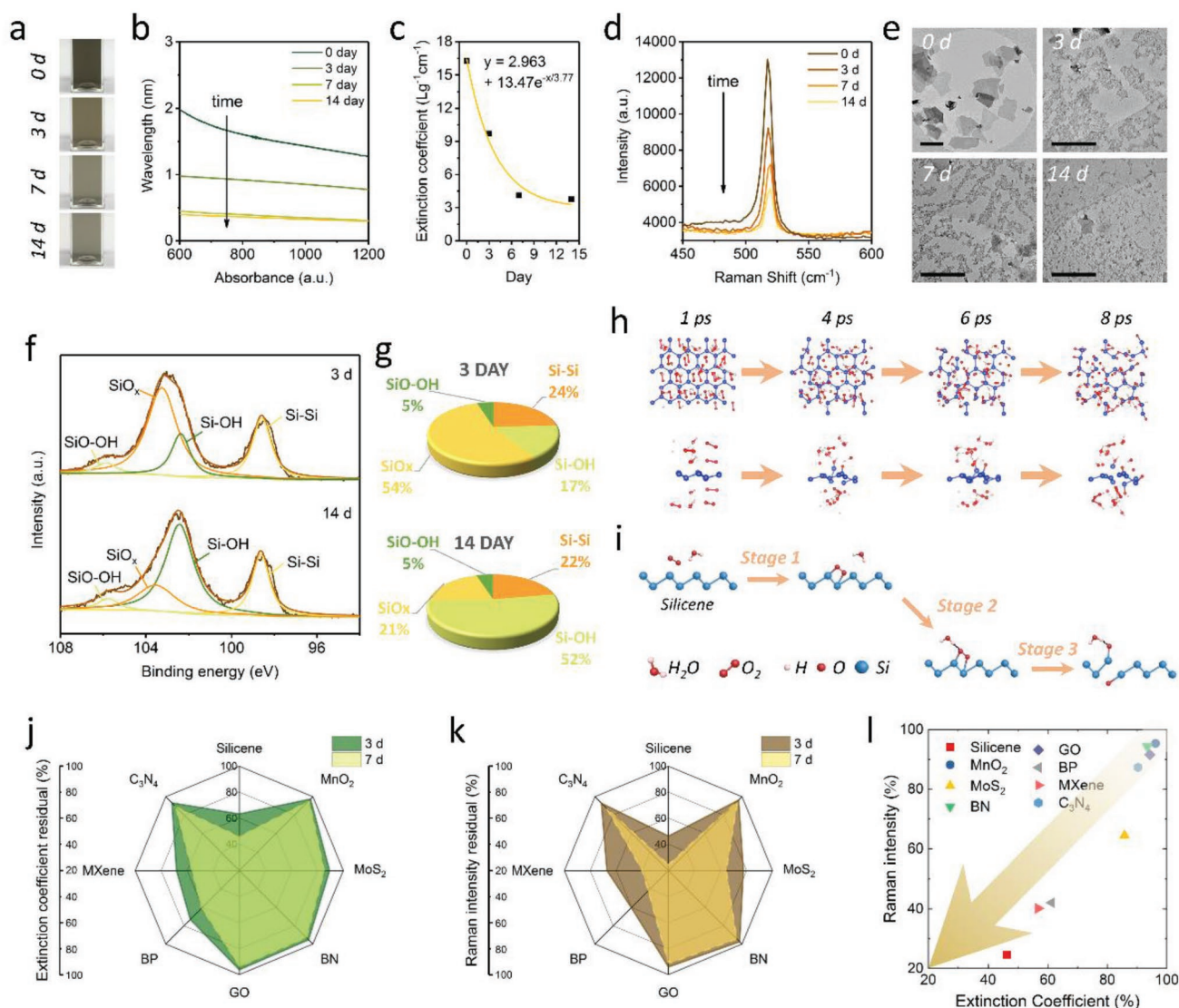


Figure 2. Composition and in vitro biodegradability of 2D silicene nanosheets. a) Photographs, b) absorbance spectra, c) mass extinction coefficient, d) Raman intensity analysis, and e) TEM images of silicene nanosheets ($80 \mu\text{g mL}^{-1}$) in varied degradation durations (0, 3, 7, and 14 days). Images share the same scale bar of 300 nm. f) XPS analysis of silicene Si 2p region in varied degradation durations (3 and 14 days). g) Quantitative analysis of bonding groups in silicene in degradation durations of 3 and 14 days. h) Representative reaction–degradation path of monolayer silicene in ambient system containing O_2 and H_2O . Minimum energy pathways (MEP) for ambient biodegradation behavior of monolayer silicene obtained by using DFT calculations. Silicene nanosheets in reaction with aqueous environment (H_2O and O_2) at temperature of 310 K. i) Oxidation and disintegration process of monolayer silicene degradation. j) Extinction coefficient residual and k) Raman intensity residual of silicene nanosheets and traditional 2D materials families (MnO_2 , MoS_2 , BN, GO, BP, MXene, C_3N_4) after storing in water for different periods of time. l) Comparisons of Raman intensity residual versus extinction coefficient residual of different 2D nanomaterials. Each symbol indicates a set of material category.

in the time course of dispersion (Figure 2c and Figure S9, Supporting Information). From the Raman scattering analysis, the degradation was found to strongly affect the fingerprint Raman peak of SNSs (located around $515\text{--}522 \text{ cm}^{-1}$), resulting in gradually reduced intensity upon increasing dispersion time interval from the beginning to the end of 14th day (Figure 2d), which might be due to the breakage of chemical bonds of SNSs in the environment containing water and oxygen.^[21] Microscopic technique was further employed to acquire more insights into the degradation of SNSs. The nanosheets of the original silicene were flat, clear, and transparent. Comparatively,

the visible small nanoparticles could be found attached on the surface of SNSs in 3 days, which was attributed to the surface oxidation of silicene by oxygen dissolved in water. It could be found that the degradation was evident as indicated by the substantial shape changes in 7 days, and the original morphology of SNSs was completely disrupted and only very few sheet-like objects could be observed in 14 days (Figure 2e).^[22]

XPS characterization was carried out to measure the oxidized silicon species after treating the SNSs suspension in 3 and 14 days (Figure 2f). Compared to the original Si 2p region of silicene (0 day) dominantly featuring a binding energy of Si–Si

atoms around 99.0 eV (Figure S4d, Supporting Information), the peaks of Si oxidation states at 102.3, 103.54, and 105.8 eV were assigned, respectively, to Si–OH (–OH terminated), SiO_x (–O terminated), and SiO–OH_x (–OOH terminated). These intense and broadened oxidation peaks of silicene occurred in 3 and 14 days by exposing to oxygen dissolved in water, suggesting a strong oxidation on SNSs framework (Figure 2f). The surface zeta potentials of degradation products gradually declined with the increasing time, indicating that the silicene did degrade over time (Figure S10, Supporting Information). Such a massive conversion of oxidation species from SiO_x (54% to 21%) to Si–OH (17% to 52%) suggests a main degradation byproduct of Si(OH)_x (Figure 2g), for example, orthosilicic acid (Si(OH)₄), which is a predominant absorbable form in human body and naturally found in diverse organs or tissues, especially featuring a high bioavailability in maintaining bone health.^[23] More importantly, silicic acid administered to human being would be efficiently metabolized from the living body by the urine or feces.^[3d,24]

To understand ambient degradation behavior of few-layered silicene nanosheet interacting with O₂ and H₂O, DFT-based molecular dynamic (MD) simulations were performed to reveal reaction mechanisms of silicene+O₂, silicene+H₂O, silicene+O₂+H₂O systems. The comparison for these MD simulations is used to reveal the different role of O₂ or H₂O in degradation reactions (Figure S11, Supporting Information). In order to speed up this process, monolayer silicene was employed for simulating degradation mechanism of FL silicene interacting with different molecules at 310 K (Figure 2h). Some important MD snapshots for silicene+O₂+H₂O, silicene+O₂, and silicene+H₂O are presented in Figures S12–S14 in the Supporting Information, respectively. The MD simulation shows that H₂O alone cannot disrupt the structure integrity of silicene sheets. Our comparison on MD simulations of silicene+O₂+H₂O and silicene+O₂ suggests that the existence of H₂O accelerates chemical bond formation between silicene and O₂. The calculation results are also in agreement with the experimental outcomes by TEM observations (Figure S15, Supporting Information). In order to clearly reveal ambient degradation mechanism of silicene interacting with O₂+H₂O, we exhibit several representative snapshots from MD simulations. A three-step reaction mechanism is revealed according to MD simulation: i) association of O₂ with three-coordinated =Si– to form a stronger Si–O bond, which is thermodynamically driven reaction. ii) A low-barrier hydrogen transfer from H₂O to =Si–O–Si– to cause O–O bond-breaking. iii) Si–Si bond-breaking to form Si–O and Si–OH. Therefore, the whole degradation process can be described as the reaction mechanism of 3(=Si–) + O₂ + H₂O → –SiO– + –Si–OH + =Si– + OH[–] → –SiO– + 2(–SiOH–) (Figure 2i).

Given that inorganic nanoparticles, unlike other traditional organic materials, generally show poor biodegradability and long-term body retention, degradation behavior of the main 2D materials were measured and then compared with silicene. The Raman intensities and extinction coefficient values of silicene and other classic inorganic nanoagents (graphene oxides (GO), black phosphorus (BP), MXenes, C₃N₄, MnO₂, MoS₂, and hBN) in different time points have been measured and analyzed in Figure 2j–l, which illustrate the noticeable advantages of silicene on degradation nature over most of the inorganic photothermal agents (Figures S16,17, Supporting Information).

The optical absorption spectra acquired on SNSs exhibit an intense and broad absorption ranging from NIR-I to NIR-II biowindow (750–1350 nm), which was unique in the inorganic materials employed as a photothermal agent (Figure 3a). Compared to the well-explored NIR-I biowindow, working in the NIR-II biowindow features two merits, the rational maximum permissible exposure (MPE) and desirable laser penetration depth.^[25] Normalized adsorption intensities over the length of the sample cell (*A/L*) at $\lambda = 1064$ nm with different concentrations (*C*) were calculated. According to the Lambert–Beer law ($A/L = \epsilon C$, where ϵ is the extinction coefficient), a linear function of *A/L* versus the concentration was obtained, and the extinction coefficient at $\lambda = 1064$ nm was determined to be 16.0 L g^{–1} cm^{–1} (Figure 3a, inset), which is higher than that of representative photoabsorption nanoagents such as graphene oxides (3.6 L g^{–1} cm^{–1}),^[26] Au nanorods (13.9 L g^{–1} cm^{–1}),^[27] and black phosphorus QDs (14.8 L g^{–1} cm^{–1}),^[28] suggesting/depicting the strong NIR-II laser absorption potential of silicene. Furthermore, the photothermal-conversion efficiency (η), another essential parameter used to estimate the photothermal performance of silicene, was calculated according to the results of time constant regarding heat conversion and the extreme steady-state temperature (Figure 3b), showing that the η value reaches 36.09% in the NIR-II biowindow, remarkably higher than that of typical Au nanorods (21%),^[27] Cu₉S₅ nanocrystals (25.7%),^[29] and Ti₃C₂ nanosheets (30.6%).^[17b]

To evaluate the photothermal-conversion performance, the aqueous suspensions of dispersed SNSs upon exposure to a 1064 nm laser were utilized to study its thermal effect. Under exposure to 1.0 W cm^{–2} of 1064 nm laser, the MPE standard for skin exposure (following the American National Standard for Safe Use of Lasers, ANSI Z136.1-2007),^[30] a relatively low SNSs concentration of 40 μ g mL^{–1} shows temperature elevation up to 47 °C in 5 min of irradiation (Figure 3c). In contrast, the temperature of water exhibits no remarkable temperature rise, elucidating that the presence of SNSs can rapidly and effectively convert NIR-II irradiation to thermal energy (Figure 3d). More detailed experiments were performed to evaluate the photothermal-conversion potential of SNSs at varied concentrations (40, 20, 10, 5 μ g mL^{–1}, and water) under NIR-II irradiation (1.0 W cm^{–2}) (Figure 3d).

To better understand the photothermal-promoted biodegradation behavior of silicene in the interactions with H₂O and O₂, we performed microcanonical molecular dynamic simulations on different temperatures (310, 333, 373, and 410 K) (Figures S19–S22, Supporting Information). On one hand, the monolayer silicene model gradually decomposes along with the Si–Si bond cleavage, as verified by internal reaction coordinate analysis. On the other hand, the simulation results at varied temperatures upon certain reaction coordinate, suggest accelerated disruption of Si–Si bonds, implying that the photothermal effect will promote the degradation of silicene topologic framework (Figure 3e).

Furthermore, the detailed experimental evaluations were performed to confirm such photothermal-induced biodegradation behavior. The SNS-dispersed aqueous suspensions exposed to NIR-II laser irradiation (10 min) with varied power densities, were employed to guarantee different temperature elevations (25, 37, 60, and 90 °C) (Figure 3f). The absorbance intensity of the

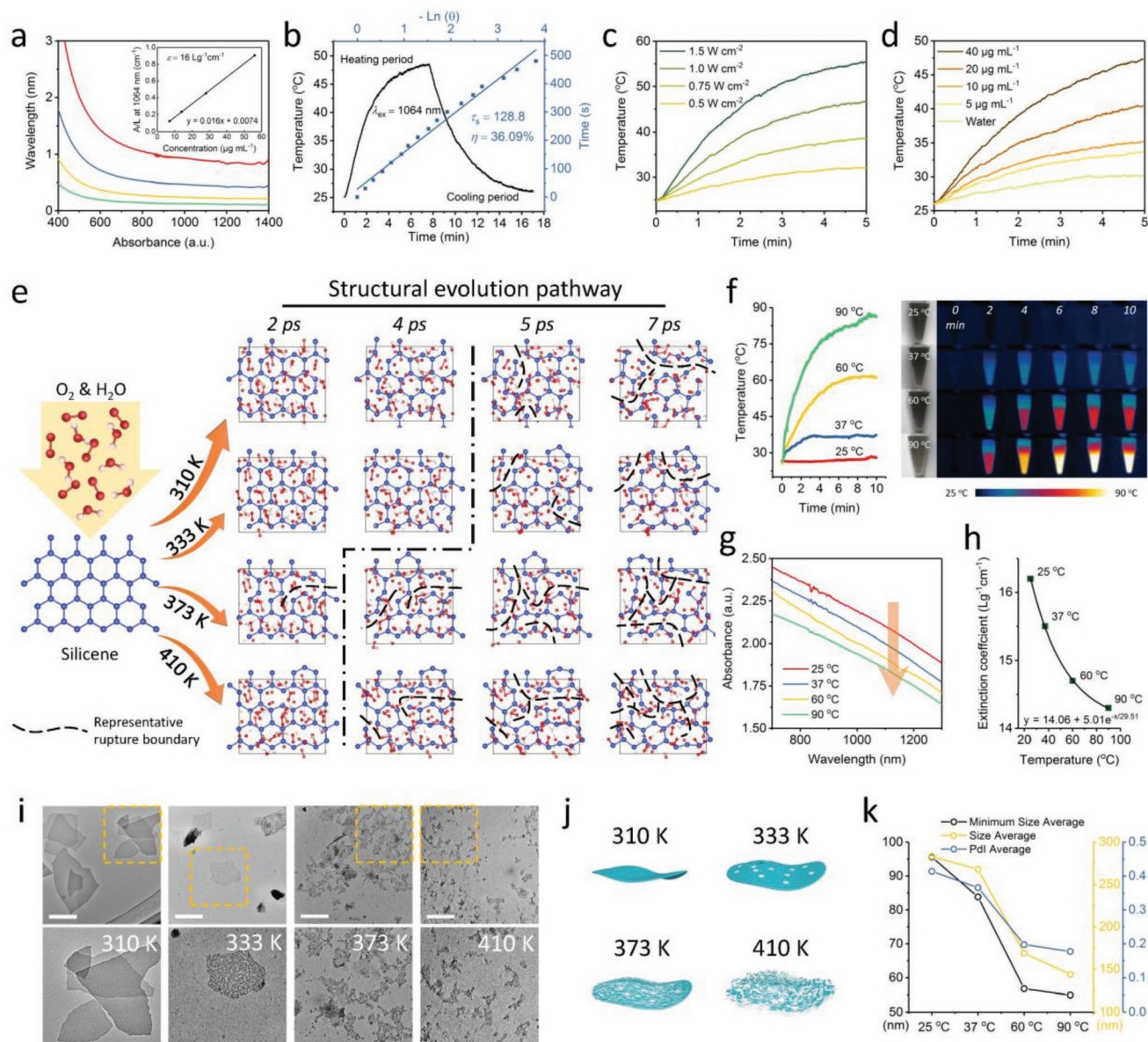


Figure 3. Photothermal-conversion performance and photothermally accelerated degradation of 2D biodegradable silicene nanosheets. a) Absorbance spectra of silicene dispersed in water at varied concentrations of silicene (from top to bottom: 56, 28, 14, and 7 $\mu\text{g mL}^{-1}$). Inset in a): Mass extinction coefficient of silicene at 1064 nm. b) Calculation of the photothermal-conversion efficiency at 1064 nm (NIR-II) laser irradiation. Black line: photothermal performance of an aqueous dispersion of silicene with NIR-II laser irradiation on (heating period) and off (cooling period). Blue line: time constant (τ_s) for the heat conversion from the system determined by linear-fitting the time-dependent data in the cooling periods. c) Photothermal-conversion heating curves of aqueous suspensions of dispersed silicene (40 $\mu\text{g mL}^{-1}$) under the irradiation of a 1064 nm (NIR-II) laser at varied power densities (0.5, 0.75, 1.0, and 1.5 W cm^{-2}). d) Photothermal-conversion heating curves of silicene-dispersed aqueous suspension under NIR-II laser irradiation (1064 nm, 1.0 W cm^{-2}) at varied concentrations (0, 5, 10, 20, and 40 $\mu\text{g mL}^{-1}$). e) Snapshots of atomic layer-structures matching the minimum energy pathways for photothermally accelerated biodegradation behavior of silicene nanosheets in the aqueous environment (H_2O and O_2) at varied temperatures (310, 333, 373, and 410 K). f) Photothermal-conversion heating curves (10 min) and the corresponding digital photographs and infrared thermal images of silicene aqueous solutions (132 $\mu\text{g mL}^{-1}$) showing varied photothermal-conversion temperatures (25, 37, 60, and 90 $^\circ\text{C}$). g) Absorbance spectra, h) mass extinction coefficient, i) TEM images with different magnifications, j) the corresponding schematic diagram for silicene degradation, and k) hydrodynamic size and monodispersity analysis of silicene aqueous solutions (132 $\mu\text{g mL}^{-1}$) at the corresponding temperatures by photothermal treatment (25, 37, 60, and 90 $^\circ\text{C}$). Images in (i) share the same scale bar of 200 nm.

SNSs in water decreases with temperature elevation (Figure 3g and Figure S23, Supporting Information). The corresponding mass extinction coefficient of 90 $^\circ\text{C}$ -treated sample declines to 14.3 $\mu\text{g mL}^{-1}$ compared with the that of 25 $^\circ\text{C}$ -treated sample at

around 16 $\mu\text{g mL}^{-1}$ (Figure 3h and Figures S24,S25, Supporting Information). TEM observation results also demonstrate such a photothermal-augmented biodegradation process. The silicene nanosheets show significant change in morphology with the

increasing of treatment temperature. At the treatment temperature of 37 °C, the flat-layered morphology became porous. Then, when the temperature was raised to 60 °C, a further evolution in the morphology occurred, which presents a gradual cleavage of silicene configuration along with a certain number of nanoscale fragments, which is attributed to the high porosity and drastic oxidation on silicene sheets. Finally at 90 °C, the majority of silicene nanosheets were converted into highly dispersed fragments with amorphous structure, where the 2D planar motif of SNSs was completely damaged (Figure 3i,j). This regular variation was further proven by dynamic light scattering (DLS) measurements. The average lateral size of SNSs samples declines with the temperature elevating, while the average PDI values drastically decreases in the course of temperature elevation (Figure 3k). These results also emphasize a thermo-dependent degradation behavior of the synthesized silicene.

Owing to the enhanced steric hindrance of organic chain molecules, the surface modification of bovine serum albumin (BSA) on as-synthesized silicene nanosheets (SNSs-BSA) guarantees a superb colloidal stability in physiological medium (Figure S26a,b, Supporting Information). The mass percentage of BSA in SNSs-BSA after surface modification was measured by thermogravimetric analysis (TGA) (Figure S26c, Supporting Information). It could be found that the coating amount of BSA on the SNSs-BSA is 5.76%. SNSs-BSA exhibits excellent colloidal dispersity and stability in a variety of simulated physiological media, including 0.9% aqueous NaCl (saline), phosphate buffered saline (PBS), fetal bovine serum (FBS), and Dulbecco's modified Eagle medium (DMEM) (Figure S27, Supporting Information).

Confocal laser scanning microscopy (CLSM) images present the effective cellular uptake of FITC-labeled SNSs-BSA after the co-incubation for 8 h, which is quantitatively supported by the flow cytometry analysis for determining the effective endocytosis amount of SNSs-BSA (Figure S28a,b, Supporting Information). An evident elevation in fluorescence intensity of FITC-labeled SNSs-BSA was measured from 0% to 78.5% (Figure S29, Supporting Information). In vitro toxicities of SNSs-BSA to cells were determined via the standard cell counting kit-8 (CCK-8) assay. Breast 4T1 cancer cells and glioma U87 cancer cells were co-incubated with SNSs-BSA at varied concentrations (0, 12.5, 25, 50, 100, and 200 $\mu\text{g mL}^{-1}$) for 24 h. SNSs-BSA exhibit insignificant effect on cell viability of either 4T1 or U87 cancer cells, even at a high concentration of 200 $\mu\text{g mL}^{-1}$ (Figure S28c, Supporting Information). Furthermore, SNSs-BSA as photothermal-conversion nanoagent for in vitro cancer-cell hyperthermia upon exposure to NIR-II laser irradiation was investigated. 4T1 cell lines were incubated with the SNSs-BSA-dispersed culture medium at the concentration of 50 $\mu\text{g mL}^{-1}$ for 8 h, then exposed to NIR-II laser of varied power densities (0, 0.25, 0.5, 0.75, 1.0, and 1.5 W cm^{-2}). It could be found that with the increase of input laser energy, more cancer cells were killed by the efficient photothermal-conversion ablation (Figure S28d, Supporting Information). In order to distinctly characterize the silicene-based photo-induced cancer-cell ablation, the potent cell apoptosis/necrosis after photothermal ablation was further demonstrated by CLSM observation (Figure S28e,f, Figure S30, and Discussion S2, Supporting Information).

To uncover the underlying mechanism of in vitro PTT utilizing SNS-NSA to kill cancer cells, the therapeutic effect was

quantitatively determined by a flow cytometry apoptosis assay based on the typical AnnexinV-FITC and propidium iodide (PI) stained protocol (Figure S28g,h, Supporting Information). The quantitative result matches well the conclusions from CCK assay and CLSM observation, as evidenced by the apoptosis of majority cells in sample of SNSs-BSA + NIR-II group, suggesting the highly effective photothermal ablation of cancer by employing SNSs-BSA as a novel silicon-based biodegradable nanoagent.

A precise study of in vivo biosafety of SNSs-BSA was introduced to investigate its clinical and translational potential. The SPF-level mice were raised and divided into groups on the basis of different experimental treatments: i) control, ii) mice with SNSs-BSA intravenously treated, and iii) mice with SNSs-BSA intravenously treated under artificial daylight (Figure 4a). In a four-week duration, the mice was recorded free of abnormality by body weight, and no significant behavioral alterations were observed in treated groups compared to control group (Figure 4b).

The histological observations of major organs (heart, liver, spleen, lung, and kidney) were collected for hematoxylin and eosin (H&E) staining (Figure 4c). No significant acute pathological toxicity and side-effects can be observed during the treatment duration for control or treated groups, depicting no marked histological abnormalities in the treated groups. In addition, the regular hematology indexes were examined (Figure 4d). It could be found that meaningless changes can be observed in the SNSs-BSA-treated groups at varied time intervals compared with the control mice. These results indicate that the SNSs-BSA have caused insignificant inflammation or infection in the treated groups. The normal blood biochemical parameters were conducted and various biomarkers were detected. All the parameters in the SNSs-BSA-treated groups at varied time intervals present no abnormality compared with the control group and such changes are of no statistical significance. Thus, the SNSs-BSA treatment does exert no passive influence on the blood biochemistry. Furthermore, since ALT, AST, ALP, UREA, CREA, and UA featuring key parameters for the kidney and liver function, the normal level of these indexes also indicates that the SNSs-BSA induce negligiblerenal and hepatic toxicity in mice model (Figure 4e).

Moreover, the excretion pathways containing urine and feces exhibit that around 12% of Si element was excreted out of mice in 48-hour intravenous injection, which demonstrates the possible mode of SNSs-BSA excreted out via the urine and feces (Figure 4f), proving the desirable in vivo biosafety for clinical translation.

On the basis of the above practices, even though the SNSs-BSA-treated mice are of exposure to artificial daylight, no significant negative impacts could be observed, which demonstrates that the SNSs-BSA induces no apparent phototoxicity. These results exhibit that SNSs-BSA are of high biocompatibility for further safe in vivo tumor nanomedicine.

Besides, fluorescence imaging was performed to analyze the distribution of SNSs-BSA in living body of mice. Figure 6g shows the ex vivo fluorescence photographs of main organs obtained at varied time intervals, where the accumulation of SNSs-BSA at tumor increased up to the maximum in 12 h. For quantitative analysis, tumors and organs were solubilized by lysis buffer to quantify the amount of accumulated SNSs-BSA. As shown in Figure S31 in the Supporting Information, time-dependent biodistribution of SNSs-BSA at tumor and

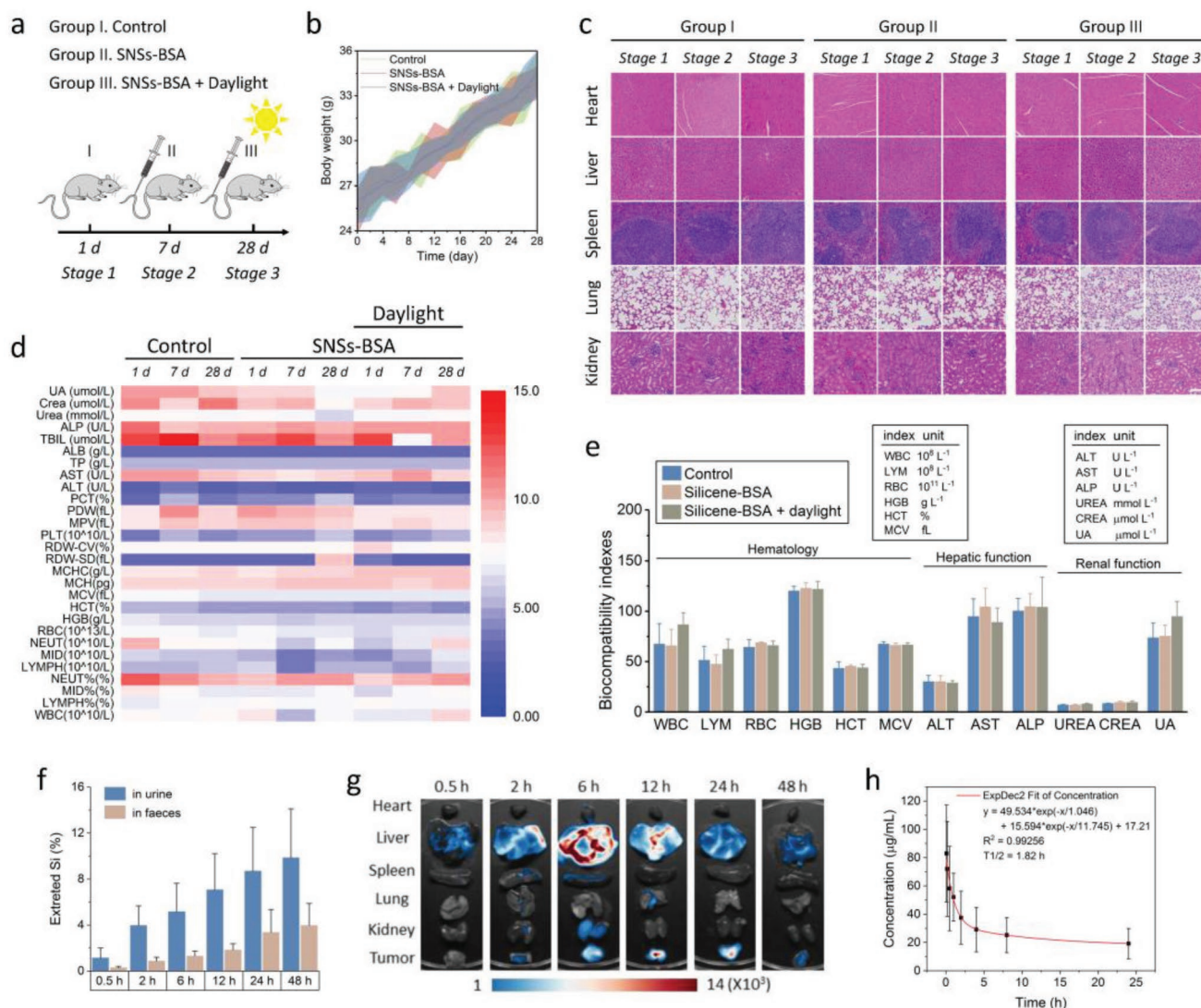


Figure 4. In vivo toxicity evaluation and pharmacokinetic and biodistribution analysis. a) Schematic diagram of in vivo toxicity evaluation model. b) Time-dependent body-weight curves of CD-1 mice within 28 days after various treatments (group I: control; group II: SNSs-BSA only; group III: SNSs-BSA + daylight). c) Histological analysis based on collecting H&E staining images of the major organs (heart, liver, spleen, lung, and kidney) of CD-1 mice in 1, 7, and 28 days (stage 1, stage 2, and stage 3) postinjection after various treatments (group I: control; group II: SNSs-BSA only; group III: SNSs-BSA + daylight). Optical images share the same scale bar (100 μm). d) Blood biochemistry and hematological parameters of CD-1 mice in 1, 7, and 28 days postinjection after various treatments (group I: control; group II: SNSs-BSA only; group III: SNSs-BSA + daylight). Optical images share the same scale bar (100 μm). e) Core hematological, hepatic, and renal biochemical parameters of CD-1 mice in 28 days post-injection under after various treatments. f) Accumulated Si (in feces and urine) excretion out of the CD-1 mice after the postinjection of SNSs-BSA for varied durations (0.5, 2, 6, 12, 24, and 48 h). g) Fluorescence images of major organs and tumor harvested from 4T1-tumor-bearing mice after post-injection of Cy5.5-labeled silicene-BSA at varied time points (0.5, 2, 6, 12, 24, and 48 h). h) The blood circulation curve of SNSs-BSA after intravenous injection into mice ($n = 3$). The half-time ($T_{1/2}$) was calculated to be ≈ 1.82 h.

major organs was measured and high signal of SNSs-BSA was observed in the tumor site, as well as reticuloendothelial systems (RES) including liver, lung, and kidney, which are compatible with the ex vivo fluorescence photographs (Figure 4g). The blood circulation half-time of SNSs-BSA in blood stream was measured to be 1.82 h (Figure 4h). Thus, the drug–light interval was determined to be 12 h between post-injection and light irradiation for the PTT treatment.

Encouraged by the in vitro high NIR-II laser absorbances, desirable photothermal-transduction effect and in vivo accumulation efficiency of SNSs-BSA, the in vivo PTT experiments were further

performed on xenograft-tumor-bearing mice (Figure 5a). After intravenous (IV) administration of SNSs-BSA/PBS (20 mg kg^{-1}), 4T1-tumor-bearing mice were exposed to 1064 nm NIR-II laser (1.0 W cm^{-2}), and the tumor-site temperatures rapidly increased from ≈ 34 to ≈ 48 $^{\circ}\text{C}$ in 10 min of therapeutic irradiation. In contrast, the tumor temperature under the NIR-II laser irradiation only exhibited slight fluctuation (Figure 5b,c).

For further in vivo phototherapeutic evaluation, the 4T1 tumor-bearing mice were randomly divided into four groups: control, SNSs-BSA (IV) only, NIR-II only, and SNSs-BSA (IV) + NIR-II. NIR laser irradiations were carried out in 12 h post-injection

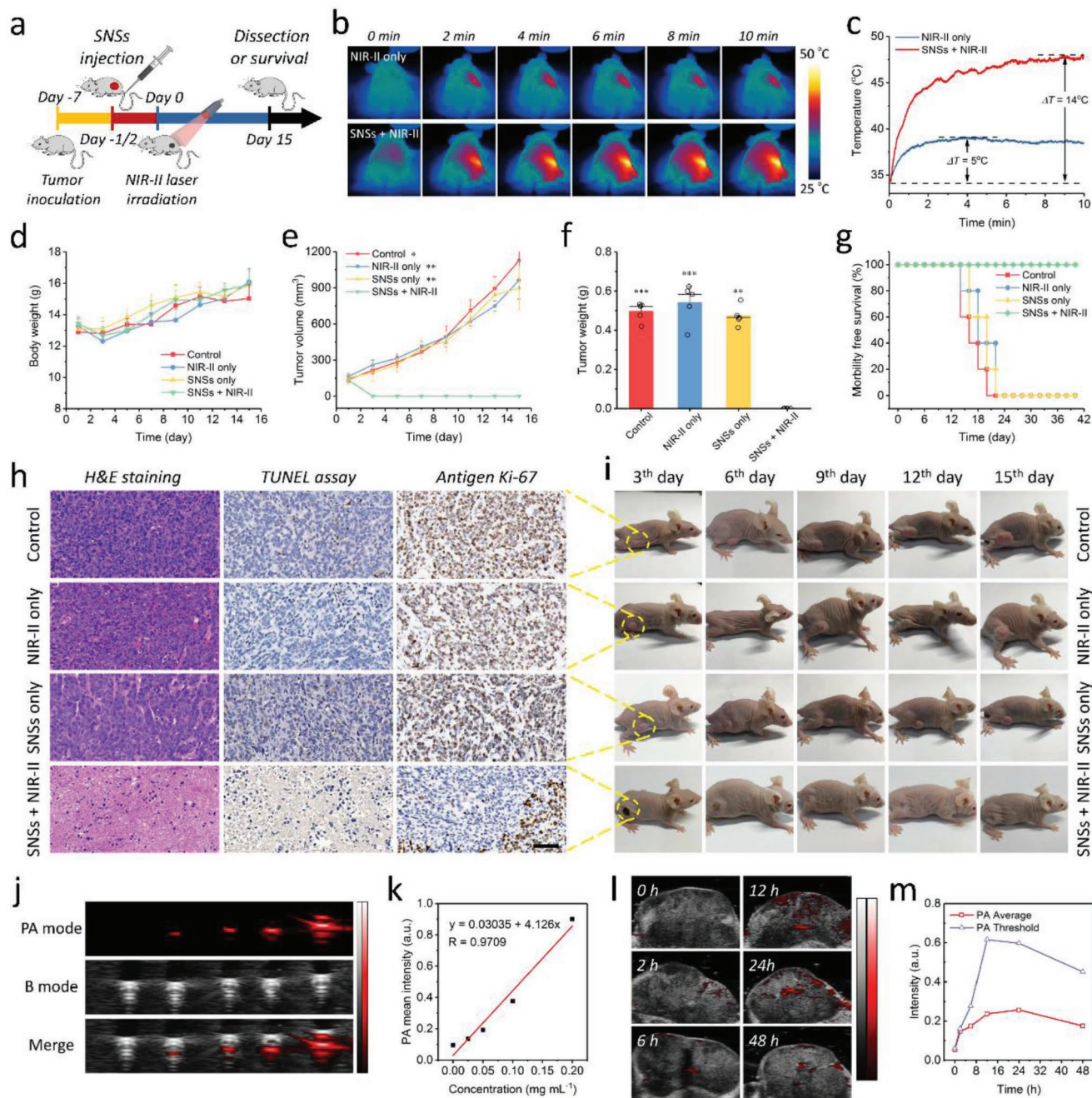


Figure 5. In vivo photothermal cancer therapy and photoacoustic imaging. a) In vivo treatment schedule of SNSs-BSA therapeutic evaluation. b) Infrared thermal images and c) the corresponding temperature elevations at the tumor regions of 4T1-tumor-bearing mice in groups of NIR-II and SNSs-BSA + NIR-II during laser irradiation. d) Time-dependent body weight curves of nude mice ($n = 5$, mean \pm SD) after different treatments (control, NIR-II only, SNSs-BSA only, and SNSs-BSA + NIR-II). The treatments were performed only once. e) In vivo 4T1 tumor proliferation curves of nude mice ($n = 5$, mean \pm SD) after various treatments. f) Tumor weights of mice 21 days after the treatments. g) Survival curves of mice after different treatments. h) H&E staining and TUNEL staining for pathological changes, and antigen Ki-67 staining for cellular proliferation in tumor sections from each group. Images share the same scale bar of 50 μm . i) Digital photographs of 4T1-tumor-bearing mice and their tumor sites in 16 days after treatments. j) In vitro PA images and k) PA values of SNSs-BSA solutions as a function of concentration (0, 0.025, 0.05, 0.1, and 0.2 mg mL^{-1} with respect to Si). l) In vivo PA value temporal evolution and m) PA images of the tumor region at different time intervals (0, 2, 6, 12, 24, and 48 h) after tail-vein injection.

(IV) of SNSs-BSA. In three days after photothermal ablation, tumors in treated group (SNSs-BSA (IV) + NIR-II) were eliminated, leaving black scars at the initial tumor regions. The

tumor volumes for each group were measured every two days (Figure 5e), and the digital photographs of tumor sites were captured every three days in a half-month duration after the

treatments (Figure 5i). Remarkably, mice in the groups of control, SNSs-BSA (IV) only, NIR-II only exhibited average life-span of 14–22 days. In contrast, all treated mice in SNSs-BSA (IV) + NIR-II group with tumors exhibited a complete tumor eradication and survived over 40 days without the tumor reoccurrence (Figure 5f,g). All the mice feature negligible weight fluctuations, thus confirming negligible negative impacts of these treatments on the health of mice (Figure 5d). H&E and TdMediated dUTP Nick-End Labeling (TUNEL) staining results show the significant necrosis of tumor tissues of SNSs-BSA (IV) + NIR-II group compared to the mice groups of control, SNSs-BSA (IV) only, and NIR-II only. The *in vivo* proliferative effect was investigated by Ki-67 antibody staining, and the SNSs-BSA (IV) + NIR-II group presented strong suppression capacity on the cell proliferation, while the other three groups exhibited nearly no passive influence on the proliferative capacity of cancer cells (Figure 5h).

Apart being a novel photothermal-transduction nanoagent to achieve high efficiency of *in vivo* tumor eradication under NIR irradiation, SNSs-BSA can also act as a robust contrast agent (CA) for photoacoustic (PA) imaging. The PA signals of a series of SNSs-BSA at varied concentrations clearly demonstrate their contrast-enhancement performances (Figure 5j,k). On the basis of these results, 4T1-tumor-bearing mice were intravenously administrated with SNSs-BSA (20 mg kg⁻¹), and PA images were obtained at varied time intervals post-injection (Figure 5l and

Figure S32, Supporting Information) under NIR irradiation. In comparison to the precontrast image, it is clear that the intensity of PA signal increased from 0.06 to 0.6 a.u. (Figure 5m), and the tumor region was gradually enlightened, exhibiting a maximum enhance in around 12 to 24 h post-injection, largely owing to the accumulation of SNSs-BSA through the enhanced permeability and retention (EPR) effect. Thereafter, the signal of the tumor region started to decline, presenting that the SNSs-BSA accumulated by tumor tissue were being gradually excreted out.

To elucidate the underlying mechanism of tumor death triggered by SNSs-BSA-based photothermal therapy, the tumors were collected to isolate primary tumor cells for flow cytometric apoptosis assay and related quantitative analysis. As expected, the proportion of apoptotic cells in certain SNSs-BSA + NIR-II laser (1.0 W cm⁻²) samples was dramatically higher than those of the groups of no treatment, SNSs-SBA only, and NIR-II laser (1.0 W cm⁻²) only (44.6% vs 5.7%, 8.1%, 5.7%, respectively), proving SNSs-BSA an efficient photothermal therapeutic agent. Furthermore, despite the similar cell apoptosis tendency showed in three core experimental group (SNSs-BSA + NIR-II laser of 0.75, 1.0, and 1.25 W cm⁻², respectively), the cells show a significantly increased apoptosis at the elevated intensities of NIR-II laser, further verifying the capacity of SNSs-BSA-based PTT modality to eliminate the malignant tumor *in vivo* (Figure 6a,b). In addition, tumor tissues were collected from

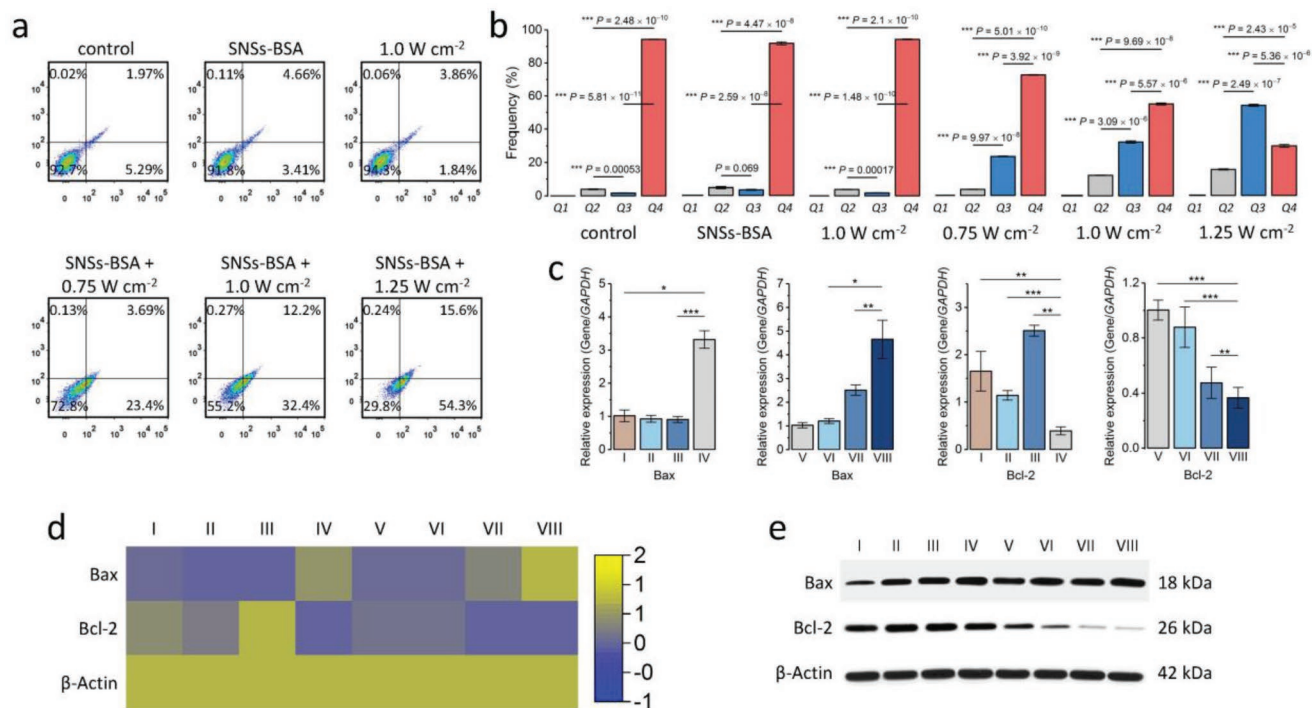


Figure 6. *In vivo* mechanism of cell death triggered by photothermal ablation based on 2D silicene as a biodegradable bio-nanoagent. a) *In vivo* flow cytometric apoptosis assay and b) the corresponding quantitative analysis of cells isolated from tumor tissues of 4T1-tumor-bearing mice under various treatments. Groups: control, SNSs-SBA only, NIR-II laser only, SNSs-SBA + NIR-II laser (0.75 W cm⁻²), SNSs-SBA + NIR-II laser (1.0 W cm⁻²) and SNSs-SBA + NIR-II laser (1.25 W cm⁻²). c) mRNA levels of Bax, Bcl-2, and beta-actin in the tumor tissues across groups (Group I: control, Group II: SNSs-BSA only, Group III: NIR-II of 1.0 W cm⁻² only, Group IV: SNSs-BSA + NIR-II of 0.1 W cm⁻², Group V: SNSs-BSA + NIR-II of 0.25 W cm⁻², Group VI: SNSs-BSA + NIR-II of 0.5 W cm⁻², Group VII: SNSs-BSA + NIR-II of 0.75 W cm⁻², and Group VIII: SNSs-BSA + NIR-II of 1.25 W cm⁻²) were analyzed by qPCR (mean ± SD, *n* = 3 for each group). d) Heatmap showing mRNA expression levels of differentially expressed genes in various groups. All data are presented as mean ± SD (*n* = 3 for each group) with **P* < 0.05, ***P* < 0.01, ****P* < 0.001 (two-tailed Student's *t*-test). e) Protein levels of Bax, Bcl-2, and beta-actin as detected by Western blot after lysis of tumor tissues in Groups I–VIII.

mice in all groups after various treatments and the expression levels of mRNA and proteins (Bax and Bcl-2) were detected by qPCR and Western blot (Figure 6c–e). Increased expression of Bax and reduced expression of Bcl-2 at both the mRNA and protein levels were observed in SNSs-BSA + NIR-II laser group but not in the other groups, which implies that photothermal-induced downregulation of Bcl-2, by activating the mitochondrial apoptotic pathway, plays a significant role in PTT-mediated cancer-cell apoptosis.^[31]

The contemporary uses of silicon-based nanomedicines for biomedical engineering has been largely limited to only serving as carriers in drug delivery systems. Though featuring intriguing physiochemical natures, the bio-related degradability and clearance of siliceous nanomaterials have been questioned worldwide, since these issues are the crucial prerequisites for the successful translation in clinics. Here, we successfully fabricated a novel kind of 2D silicene nanosheets (SNSs) with a marked degradable nature, and demonstrated their in vivo highly efficient cancer phototherapy of mouse tumor xenografts in NIR-II biowindow. Such a 2D silicene was synthesized by a facile and scalable two-step liquid/gas exfoliation method combining stepwise mild oxidation-triggered delamination and gasification-induced exfoliation procedures. The ultrathin, lateral-nanosized silicene exhibited extraordinarily high photothermal conversion efficiency (36.08% at 1064 nm of NIR-II biowindow), as well as concomitant high photoacoustic contrast.

The SNSs intrinsically feature respectable ambient degradability and potent photothermal-promoted degradability. Combining with density functional theory (DFT) analysis, the mechanisms of the interactions between silicene and related molecules such as water and oxygen, and the resultant degradations were revealed under the specific simulated physiological condition. Especially, the internal mechanism of cell death triggered by PTT based on 2D silicene as photo-nanoagent was also revealed. This work significantly broadens the application prospects of 2D silicene by rationally designing their multifunctionality and exploring related physiochemical properties, especially on phototherapy of cancer.

Supporting Information

Supporting Information is available from the Wiley Online Library or from the author.

Acknowledgements

The authors greatly acknowledge the financial support from National Key Research and Development Program of China (Grant No. 2016YFA0203700), National Natural Science Foundation of China (Grant No. 51722211, 21835007, and 51672303), and Program of Shanghai Academic Research Leader (Grant No. 18XD1404300). Animal experiment procedures were in agreement with the guidelines of the Regional Ethics Committee for Animal Experiments and the care regulations approved by the administrative committee of laboratory animals of Fudan University.

Conflict of Interest

The authors declare no conflict of interest.

Keywords

2D topology, biodegradation, nanomedicine, silicene, wet-chemical exfoliation

Received: May 11, 2019

Revised: June 18, 2019

Published online:

- [1] M. Jaroniec, *Nat. Chem.* **2009**, *1*, 166.
- [2] a) N. Yamaji, G. Sakurai, N. Mitani-Ueno, J. F. Ma, *Proc. Natl. Acad. Sci. USA* **2015**, *112*, 11401; b) B. Hidding, *Science* **2018**, *360*, 489.
- [3] a) J. F. Zimmerman, R. Parameswaran, G. Murray, Y. Wang, M. Burke, B. Tian, *Sci. Adv.* **2016**, *2*, e1601039; b) J. Viventi, D. H. Kim, J. D. Moss, Y. S. Kim, J. A. Blanco, N. Annetta, A. Hicks, J. Xiao, Y. Huang, D. J. Callans, J. A. Rogers, B. Litt, *Sci. Transl. Med.* **2010**, *2*, 24ra22; c) E. Tasciotti, X. Liu, R. Bhavane, K. Plant, A. D. Leonard, B. K. Price, M. M. Cheng, P. Decuzzi, J. M. Tour, F. Robertson, M. Ferrari, *Nat. Nanotechnol.* **2008**, *3*, 151; d) J. H. Park, L. Gu, G. von Maltzahn, E. Ruoslahti, S. N. Bhatia, M. J. Sailor, *Nat. Mater.* **2009**, *8*, 331; e) M. M. Orosco, C. Pacholski, M. J. Sailor, *Nat. Nanotechnol.* **2009**, *4*, 255; f) H. Kim, H. Jang, B. Kim, M. K. Kim, D. S. Wie, H. S. Lee, D. R. Kim, C. H. Lee, *Sci. Adv.* **2018**, *4*, eaau6972; g) B. Kim, H. B. Pang, J. Kang, J. H. Park, E. Ruoslahti, M. J. Sailor, *Nat. Commun.* **2018**, *9*, 1969.
- [4] a) Y. Zhu, J. Shi, W. Shen, X. Dong, J. Feng, M. Ruan, Y. Li, *Angew. Chem., Int. Ed.* **2005**, *44*, 5083; b) D. Zhao, J. Feng, Q. Huo, N. Melosh, G. H. Fredrickson, B. F. Chmelka, G. D. Stucky, *Science* **1998**, *279*, 548; c) G. Valenti, E. Rampazzo, S. Bonacchi, L. Petrizza, M. Marcaccio, M. Montalti, L. Prodi, F. Paolucci, *J. Am. Chem. Soc.* **2016**, *138*, 15935; d) N. Manuchehrabadi, Z. Gao, J. Zhang, H. L. Ring, Q. Shao, F. Liu, M. McDermott, A. Fok, Y. Rabin, K. G. Brockbank, M. Garwood, C. L. Haynes, J. C. Bischof, *Sci. Transl. Med.* **2017**, *9*, eaah4586; e) K. Ma, Y. Gong, T. Aubert, M. Z. Turker, T. Kao, P. C. Doerschuk, U. Wiesner, *Nature* **2018**, *558*, 577.
- [5] a) L. Tao, E. Cinquanta, D. Chiappe, C. Grazianetti, M. Fanciulli, M. Dubey, A. Molle, D. Akinwande, *Nat. Nanotechnol.* **2015**, *10*, 227; b) B. Lalmi, H. Oughaddou, H. Enriquez, A. Kara, S. Vizzini, B. Ealet, B. Aufray, *Appl. Phys. Lett.* **2010**, *97*, 223109; c) L. Meng, Y. Wang, L. Zhang, S. Du, R. Wu, L. Li, Y. Zhang, G. Li, H. Zhou, W. A. Hofer, H. J. Gao, *Nano Lett.* **2013**, *13*, 685.
- [6] C. C. Liu, W. Feng, Y. Yao, *Phys. Rev. Lett.* **2011**, *107*, 076802.
- [7] C. Xu, G. Luo, Q. Liu, J. Zheng, Z. Zhang, S. Nagase, Z. Gao, J. Lu, *Nanoscale* **2012**, *4*, 3111.
- [8] F. Liu, C. C. Liu, K. Wu, F. Yang, Y. Yao, *Phys. Rev. Lett.* **2013**, *111*, 066804.
- [9] A. Molle, C. Grazianetti, L. Tao, D. Taneja, M. H. Alam, D. Akinwande, *Chem. Soc. Rev.* **2018**, *47*, 6370.
- [10] a) H. Jamgotchian, Y. Colignon, N. Hamzaoui, B. Ealet, J. Y. Hoarau, B. Aufray, J. P. Biberian, *J. Phys.: Condens. Matter* **2012**, *24*, 172001; b) B. Feng, Z. Ding, S. Meng, Y. Yao, X. He, P. Cheng, L. Chen, K. Wu, *Nano Lett.* **2012**, *12*, 3507; c) Y. Du, J. Zhuang, J. Wang, Z. Li, H. Liu, J. Zhao, X. Xu, H. Feng, L. Chen, K. Wu, X. Wang, S. X. Dou, *Sci. Adv.* **2016**, *2*, e1600067.
- [11] D. Chiappe, E. Scalise, E. Cinquanta, C. Grazianetti, B. van den Broek, M. Fanciulli, M. Houssa, A. Molle, *Adv. Mater.* **2014**, *26*, 2096.
- [12] T. Aizawa, S. Suehara, S. Otani, *J. Phys. Chem. C* **2014**, *118*, 23049.
- [13] A. Fleurence, R. Friedlein, T. Ozaki, H. Kawai, Y. Wang, Y. Yamada-Takamura, *Phys. Rev. Lett.* **2012**, *108*, 245501.
- [14] A. Molle, J. Goldberger, M. Houssa, Y. Xu, S. C. Zhang, D. Akinwande, *Nat. Mater.* **2017**, *16*, 163.

- [15] a) H. Lin, Y. Chen, J. Shi, *Adv. Sci.* **2018**, *5*, 1800518; b) K. Huang, Z. Li, J. Lin, G. Han, P. Huang, *Chem. Soc. Rev.* **2018**, *47*, 5109; c) B. Anasori, M. R. Lukatskaya, Y. Gogotsi, *Nat. Rev. Mater.* **2017**, *2*, 16098.
- [16] C. Xu, L. Wang, Z. Liu, L. Chen, J. Guo, N. Kang, X. L. Ma, H. M. Cheng, W. Ren, *Nat. Mater.* **2015**, *14*, 1135.
- [17] a) H. Lin, Y. Wang, S. Gao, Y. Chen, J. Shi, *Adv. Mater.* **2018**, *30*, 1703284; b) H. Lin, X. Wang, L. Yu, Y. Chen, J. Shi, *Nano Lett.* **2017**, *17*, 384; c) H. Lin, S. Gao, C. Dai, Y. Chen, J. Shi, *J. Am. Chem. Soc.* **2017**, *139*, 16235.
- [18] a) S. M. Pratik, A. Nijamudheen, A. Datta, *Chem. - Eur. J.* **2015**, *21*, 18454; b) H. Nakano, T. Mitsuoka, M. Harada, K. Horibuchi, H. Nozaki, N. Takahashi, T. Nonaka, Y. Seno, H. Nakamura, *Angew. Chem., Int. Ed.* **2006**, *45*, 6303; c) J. Liu, Y. Yang, P. Lyu, P. Nachtigall, Y. Xu, *Adv. Mater.* **2018**, *30*, 1800838.
- [19] M. Q. Arguilla, N. D. Cultrara, M. R. Scudder, S. Jiang, R. D. Ross, J. E. Goldberger, *J. Mater. Chem. C* **2017**, *5*, 11259.
- [20] B. L. Allen, G. P. Kotchey, Y. Chen, N. V. Yanamala, J. Klein-Seetharaman, V. E. Kagan, A. Star, *J. Am. Chem. Soc.* **2009**, *131*, 17194.
- [21] R. Kurapati, C. Backes, C. Menard-Moyon, J. N. Coleman, A. Bianco, *Angew. Chem., Int. Ed.* **2016**, *55*, 5506.
- [22] R. Kurapati, L. Muzi, A. P. R. De Garibay, J. Russier, D. Voiry, I. A. Vacchi, M. Chhowalla, A. Bianco, *Adv. Funct. Mater.* **2017**, *27*, 1605176.
- [23] E. M. Carlisle, *Science* **1970**, *167*, 279.
- [24] J. F. Popplewell, S. J. King, J. P. Day, P. Ackrill, L. K. Fifield, R. G. Cresswell, M. L. di Tada, K. Liu, *J. Inorg. Biochem.* **1998**, *69*, 177.
- [25] A. N. Bashkatov, E. A. Genina, V. I. Kochubey, V. V. Tuchin, *J. Phys. D: Appl. Phys.* **2005**, *38*, 2543.
- [26] K. Yang, S. Zhang, G. Zhang, X. Sun, S. T. Lee, Z. Liu, *Nano Lett.* **2010**, *10*, 3318.
- [27] J. Zeng, D. Goldfeld, Y. Xia, *Angew. Chem., Int. Ed.* **2013**, *52*, 4169.
- [28] Z. B. Sun, H. H. Xie, S. Y. Tang, X. F. Yu, Z. N. Guo, J. D. Shao, H. Zhang, H. Huang, H. Y. Wang, P. K. Chu, *Angew. Chem., Int. Ed.* **2015**, *54*, 11526.
- [29] Q. Tian, F. Jiang, R. Zou, Q. Liu, Z. Chen, M. Zhu, S. Yang, J. Wang, J. Wang, J. Hu, *ACS Nano* **2011**, *5*, 9761.
- [30] X. Ding, C. H. Liow, M. Zhang, R. Huang, C. Li, H. Shen, M. Liu, Y. Zou, N. Gao, Z. Zhang, Y. Li, Q. Wang, S. Li, J. Jiang, *J. Am. Chem. Soc.* **2014**, *136*, 15684.
- [31] E. Miyako, T. Deguchi, Y. Nakajima, M. Yudasaka, Y. Hagihara, M. Horie, M. Shichiri, Y. Higuchi, F. Yamashita, M. Hashida, Y. Shigeri, Y. Yoshida, S. Iijima, *Proc. Natl. Acad. Sci. USA* **2012**, *109*, 7523.